ORIGINAL PAPER

The Fe–C–O–H–N system at 6.3–7.8 GPa and 1200–1400 °C: implications for deep carbon and nitrogen cycles

Alexander G. Sokol[1,2] · Anatoly A. Tomilenko[1] · Taras A. Bul'bak[1] · Alexey N. Kruk[1,2] · Pavel A. Zaikin[3] ·
Ivan A. Sokol[1] · Yurii V. Seryotkin[1,2] · Yury N. Palyanov[1,2]

Abstract

Interactions in a Fe–C–O–H–N system that controls the mobility of siderophile nitrogen and carbon in the Fe^0-saturated upper mantle are investigated in experiments at 6.3–7.8 GPa and 1200–1400 °C. The results show that the γ-Fe and metal melt phases equilibrated with the fluid in a system unsaturated with carbon and nitrogen are stable at 1300 °C. The interactions of Fe_3C with an N-rich fluid in a graphite-saturated system produce the ε-Fe_3N phase (space group $P6_3/mmc$ or $P6_322$) at subsolidus conditions of 1200–1300 °C, while N-rich melts form at 1400 °C. At IW- and MMO-buffered hydrogen fugacity (fH_2), fluids vary from NH_3- to H_2O-rich compositions ($NH_3/N_2 > 1$ in all cases) with relatively high contents of alkanes. The fluid derived from N-poor samples contains less H_2O and more carbon which mainly reside in oxygenated hydrocarbons, i.e., alcohols and esters at MMO-buffered fH_2 and carboxylic acids at unbuffered fH_2 conditions. In unbuffered conditions, N_2 is the principal nitrogen host ($NH_3/N_2 \leq 0.1$) in the fluid equilibrated with the metal phase. Relatively C- and N-rich fluids in equilibrium with the metal phase (γ-Fe, melt, or Fe_3N) are stable at the upper mantle pressures and temperatures. According to our estimates, the metal/fluid partition coefficient of nitrogen is higher than that of carbon. Thus, nitrogen has a greater affinity for iron than carbon. The general inference is that reduced fluids can successfully transport volatiles from the metal-saturated mantle to metal-free shallow mantle domains. However, nitrogen has a higher affinity for iron and selectively accumulates in the metal phase, while highly mobile carbon resides in the fluid phase. This may be a controlling mechanism of the deep carbon and nitrogen cycles.

Keywords Mantle · Metal · Fluid · Carbon · Nitrogen · Hydrocarbons · Gas chromatography–mass spectrometry

Communicated by Hans Keppler.

✉ Alexander G. Sokol
sokola@igm.nsc.ru

1 V.S. Sobolev Institute of Geology and Mineralogy, Siberian Branch of the Russian Academy of Sciences, 3, Koptyug ave, Novosibirsk 630090, Russia

2 Novosibirsk State University, 2, Pirogov str, Novosibirsk 630090, Russia

3 N.N. Vorozhtsov Novosibirsk Institute of Organic Chemistry, Siberian Branch of the Russian Academy of Sciences, 9, Lavrentiev ave., Novosibirsk 630090, Russia

Introduction

Interactions between metal, silicate, carbonate and fluid phases directly influenced the geochemical differentiation of the early Earth, the formation of its metallic core and atmosphere, magma generation, as well as the nucleation and growth of diamonds (Kuramoto and Matsui 1996; Kuramoto 1997; Dasgupta and Walker 2008; Hirschmann and Dasgupta 2009; Dasgupta and Hirschmann 2010; Rohrbach and Schmidt 2011; Hirschmann 2012; Dasgupta et al. 2013a; Palyanov et al. 2013; Rohrbach et al. 2014). In particular, the solution behavior of carbon and nitrogen, and their partitioning between metallic phases and fluid likely had a tremendous influence on the inventory and origin of deep Earth volatiles.

Carbon and nitrogen mostly reside in the silicate, metal and fluid phases of the reduced mantle at the standard heat flux 40 mW/m² and oxygen fugacity (fO_2) near or below

the iron–wüstite (IW) equilibrium (Shcheka et al. 2006; Lord et al. 2009; Dasgupta 2013; Roskosz et al. 2013; Li et al. 2013; Luth 2014). Out of these phases, the solubilities of C and N are the lowest (10 and 200 ppm, respectively) in main peridotitic silicates (Shcheka et al. 2006; Li et al. 2013). The high affinities of carbon and nitrogen for iron are expected to maintain their preferable dissolution in solid iron, iron carbides, iron nitrides and melt (Hashizume et al. 1997; Miyazaki et al. 2004; Dasgupta et al. 2013; Kadik et al. 2013; Roskosz et al. 2013; Li et al. 2016a, b; Dalou et al. 2017). This inference is supported by the presence of Fe^0 and Fe–Ni alloys, as well as iron carbide and nitride species, in mantle-derived diamonds (Sobolev et al. 1981; Stachel et al. 1998; Jacob et al. 2004; Kaminsky and Wirth 2011, 2017; Smith et al. 2016). According to experimental evidence, carbon may be dissolved in the metal phase of the deep mantle and stored in Fe_3C or Fe_7C_3 carbides (Dasgupta and Hirschmann 2010; Frost and McCammon 2008; Lord et al. 2009), at carbon abundances of ~ 20–120 ppm C (MORB source) and 300–800 ppm C (OIB source), respectively, which are characteristic of the shallow mantle (Marty 2012). As shown by Sokol et al. (2017a), melts rich in C and N are stable in the Fe–Fe_3C–Fe_3N system within a large range of compositions, at pressures and temperatures corresponding to the limit of metal-phase precipitation in the mantle, which presumably occurs at a depth of ~ 250 km (Frost et al. 2004; Rohrbach and Schmidt 2011). The complete dissolution of 20 ppm C and 1 ppm N available in the mantle depleted in volatiles (Marty 2012; Dasgupta et al. 2013a) in 0.1 wt.% iron contained in rock can produce austenite (γ-Fe) + liquid. Greater amounts of C (250 ppm) and N (100 ppm) in the enriched mantle (Dasgupta et al. 2013a; Li and Keppler 2014) dissolve with the formation of C- and N-rich melts, and minor amounts of iron carbide (Fe_3C). In the presence of Ni and S, iron carbide loses its stability, while metal melt becomes stable in a large range of compositions (Strong and Chrenko 1971; Hasterok and Chapman 2011; Rohrbach et al. 2014; Bataleva et al. 2016).

At fO_2 near or below IW, silicate melts cannot form in the metal-saturated mantle and host C and N at the standard heat flux because the solidus of peridotite in the presence of reduced fluids is ~ 100 °C above the $T_p = 1300$ °C adiabat (Fig. 1) (Taylor and Green 1988; Hasterok and Cheapmann 2011; Litasov et al. 2014); thus, they cannot participate in deep carbon and nitrogen cycles. However, the equilibria between silicate melt and molten metal, which can occur at $T \geq 1600$ °C, have important implications for magma ocean processes (Abe 1997; Solomatov 2000; Dasgupta 2013). All available experimental data suggest that C partitions more strongly into metal than N in this kind of equilibrium (Dasgupta et al. 2013; Kadik
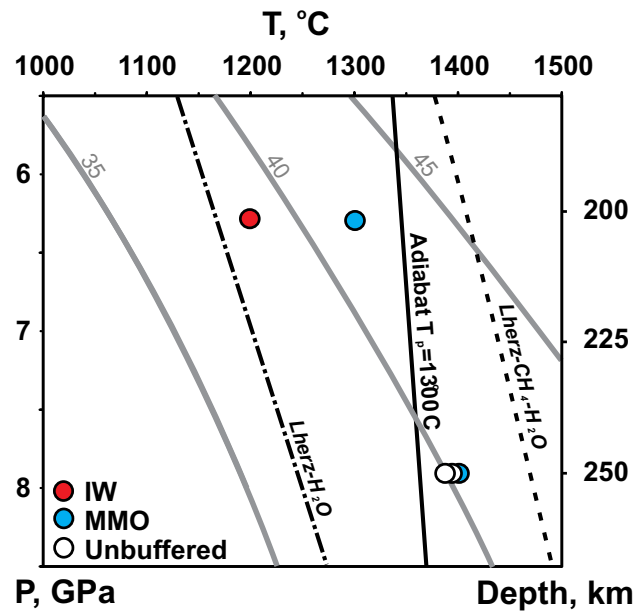

Fig. 1 *P–T* conditions of experiments. Red and blue circles mark, respectively, runs with fH_2 buffered by IW (Fe–FeO) and MMO (Mo–MoO_2) equilibria; open circles mark unbuffered runs. Gray thick lines are continental geotherms (heat flux in mW/m²); black line is mantle adiabat for a potential temperature of 1300 °C according to Hasterok and Chapman (2011). The Lherz–H_2O line is the water-saturated lherzolite solidus from Wyllie and Ryabchikov (2000); the Lherz–CH_4–H_2O line is the lherzolite solidus in the presence of a reduced C–H–O fluid at fO_2 of IW (Litasov et al. 2014)

et al. 2013; Roskosz et al. 2013; Li et al. 2016a, b; Dalou et al. 2017).

Hitherto, fluids have often remained overlooked in studies of N and C partitioning between main host phases. Meanwhile, the key role of reduced fluids as C and N hosts is consistent with the presence of hydrocarbon- and nitrogen-bearing species found in inclusions in diamonds and other mantle-derived minerals (Tomilenko et al. 1997, 2001; Smith et al. 2016; Sobolev 2017). Highly mobile mantle fluids can bridge the C and N flux between mantle reservoirs and carry the carbon required for diamond formation (Stachel and Luth 2015). According to our recent experimental results (Sokol et al. 2017b), most of carbon in the N-poor C–O–H–N fluids at fO_2 near the IW equilibrium resides in C_1–C_4 alkanes (all other components being in trace amounts), while methanimine (CH_3N) is the major nitrogen host. N-rich fluids with the same fO_2 store nitrogen and carbon in ammonia (NH_3) and N_2, and in light alkanes, respectively (Li and Keppler 2014; Sokol et al. 2017c).

Thus, the fluid–metal interactions that affect the composition of both phases may control the fate of carbon and nitrogen in the metal-saturated mantle at temperatures below the solidus of mantle peridotite. These interactions may have influenced the formation of the metallic core and

atmosphere of the young Earth. However, although being crucially important, they have never been the subject of special research. In this study, experiments at 6.3–7.8 GPa and 1200–1400 °C (Fig. 1) are applied for the first time to investigate the phase relations in the Fe–C–O–H–N system, determine the composition of fluids equilibrated with the metal phase, and estimate the iron affinities of carbon and nitrogen.

Experimental and analytical techniques

Starting materials

Nitrogen-bearing fluids were generated using chemical-grade melamine ($C_3H_6N_6$) as the starting material (Table 1). The material was placed on the bottom of Pt capsules with a 2- or 3-mm-thick outer diameter and a wall thickness of 0.2 mm. The charges were either saturated or not with respect to graphite. In the latter case, the Fe^0 interactions with fluids were studied using cylinders of > 99.99% pure iron, 1 mm in diameter, and insulated from the capsule walls by a layer of SiO_2 (> 99.99%). The graphite-saturated runs simulated Fe_3C–fluid interactions and used iron carbide (X-ray tested) synthesized at 6.3 GPa and 1400 °C from iron and graphite (both > 99.99% pure). Pieces of iron carbide, no more than 0.7 mm in diameter, were placed in capsules and insulated with > 99.9999% pure graphite. The starting iron powders used for all charges were cleaned from oxygen by annealing for 1 h in a stream of hydrogen at 600 °C. However, some amounts of oxides may have formed on metal particles even after cleaning. Graphite, which occupied most of the graphite-saturated charge volume, was dried at 110 °C for at least 30 days. Pre-dried graphite contained 700 ppm CO_2 and 700 ppm H_2O, as determined by the chromatography of gases extracted during graphite annealing at 600°C in

a U-shaped quartz cell (Sokol et al. 2017a). All initial powders were stored in a vacuum desiccator at ~ 100 mbar. The capsules containing the starting materials were arc-welded using a Lampert Werktechnik GmbH PUK-4U (Germany) impulse micro-welding tool.

High-pressure apparatus

Experiments at 6.3 and 7.8 GPa were carried out in a split-sphere multi-anvil high-pressure apparatus (Palyanov et al. 2010). Pressure was calibrated by recording the change in the resistance of Bi at 2.55 GPa and PbSe at 4.0 and 6.8 GPa at room temperature and by bracketing the graphite–diamond equilibrium at high temperatures. Temperature was monitored in each experiment using a $PtRh_6/PtRh_{30}$ thermocouple calibrated at 6.3 and 7.8 GPa using the melting points of Al, Ag, Ni and Pt. Pressure and temperature were measured to an accuracy of ± 0.1 GPa and ± 20 °C (Palyanov et al. 2010; Sokol et al. 2015). The capsules charged with the substances of the Fe–C–O–H–N system were quenched under isobaric conditions at a rate of 200 deg/s. As shown by detailed studies of the cooling rate effect on fluid compositions (Li and Keppler 2014; Sokol et al. 2017c), cooling from 1200 to 1400 °C to room temperature at 200 deg/s can provide quenching and furnish reliable evidence of the fluid compositions at the applied P–T conditions.

The run durations from 2 to 7 h (Table 1) were chosen because equilibrium fluids rich in hydrocarbons (HC) in the C–O–H–N experimental system at 6.3 GPa and 1100–1400 °C form in at least 2 h (Sokol et al. 2017a, b). The comparison of the new data with published evidence obtained from experiments of the same duration and P–T conditions, but in a simplified C–O–H–N system, revealed the effect of the metal phase on the fluid composition.

Hydrogen fugacity was buffered by the IW (Fe–FeO) and MMO (Mo–MoO_2) equilibria using a modified

Table 1 Fe–C–O–H–N system: charge composition and run conditions

Run #	Compositions (mg)					Fe/C	Fe/N	fH_2	P (GPa)	T (°C)	Time (h)	Me phase
	Graphite	Fe_3C	Fe	$C_3H_6N_6$	SiO_2							
1882_2_1	–	–	10.2	0.7	15.3	51	22	MMO	6.3	1300	2	L
1882_2_2	–	–	10.2	0.5	15.4	71	31	MMO	6.3	1300	2	γ-Fe
1365_3_1	21.9	12.1	–	2.1	–	C.S	8	IW	6.3	1200	7	ε-Fe_3N
1365_3_2	25.4	12.1	–	2.4	–	C.S	7	IW	6.3	1200	7	ε-Fe_3N
1801_2_2	24	12.3	–	1.2	–	C.S	14	MMO	6.3	1300	7	ε-Fe_3N
1778_2_1	15.4	12.6	–	2.2	–	C.S	8	MMO	6.3	1300	7	ε-Fe_3N
1796_2_2	20.7	12.3	–	2	–	C.S	9	MMO	7.8	1400	2	L
998_7_3	19	11.4	–	0.4	–	C.S	40	–	7.8	1400	5	L
1878_2_2	20.8	11.9	–	0.7	–	C.S	24	–	7.8	1400	5	L

Fe/C and Fe/N are weight ratios in the charge

C.S. carbon-saturated, fH_2 hydrogen buffer, *MMO* Mo–MoO_2, IW = Fe–FeO, *L* quenched melt (liquid)

double-capsule technique, with inner Pt capsules placed inside thick-walled Fe or Mo outer capsules with talc insulation (Sokol et al. 2009). Hydrogen was generated by the reaction of water (released by talc decomposition) with Fe or Mo from the outer capsule. The flow of hydrogen between the outer and inner capsules maintained stable fH$_2$ in the charge. The outer capsule walls were checked after each run for the presence of MoO$_2$ or FeO oxides. Our previous experiments at 6.3 GPa and 1300–1400 °C (Sokol et al. 2017c) showed that fH$_2$ buffering can maintain invariable compositions of HC and C/H ratios in fluids as the run duration increased from 1 min to 7 h with this technique, thus proving its workability at the applied P–T–τ parameters. For more details of the double-capsule

technique, see Luth (1989). In the absence of an external buffer, fH$_2$ in samples was at water maximum (Sokol et al. 2017c).

The oxygen fugacity in the samples was estimated to be near IW, using the EMPA oxygen contents in metal phases, which ranged from 0.4 wt.% in the case of fH$_2$ buffering to 0.8 wt.% in the runs with non-buffered fH$_2$ (Tables 1, 2). As we showed in another study (Sokol et al. 2017a), the 0.4–0.5 wt.% O contents in the metal phases of the Fe–Fe$_3$C–Fe$_3$N system at 7.8 GPa and 1350 °C correspond to equilibrium, when FeO appears in the system. This inference is supported by the presence of small (within 10 µm) FeO grains (Fig. 2).
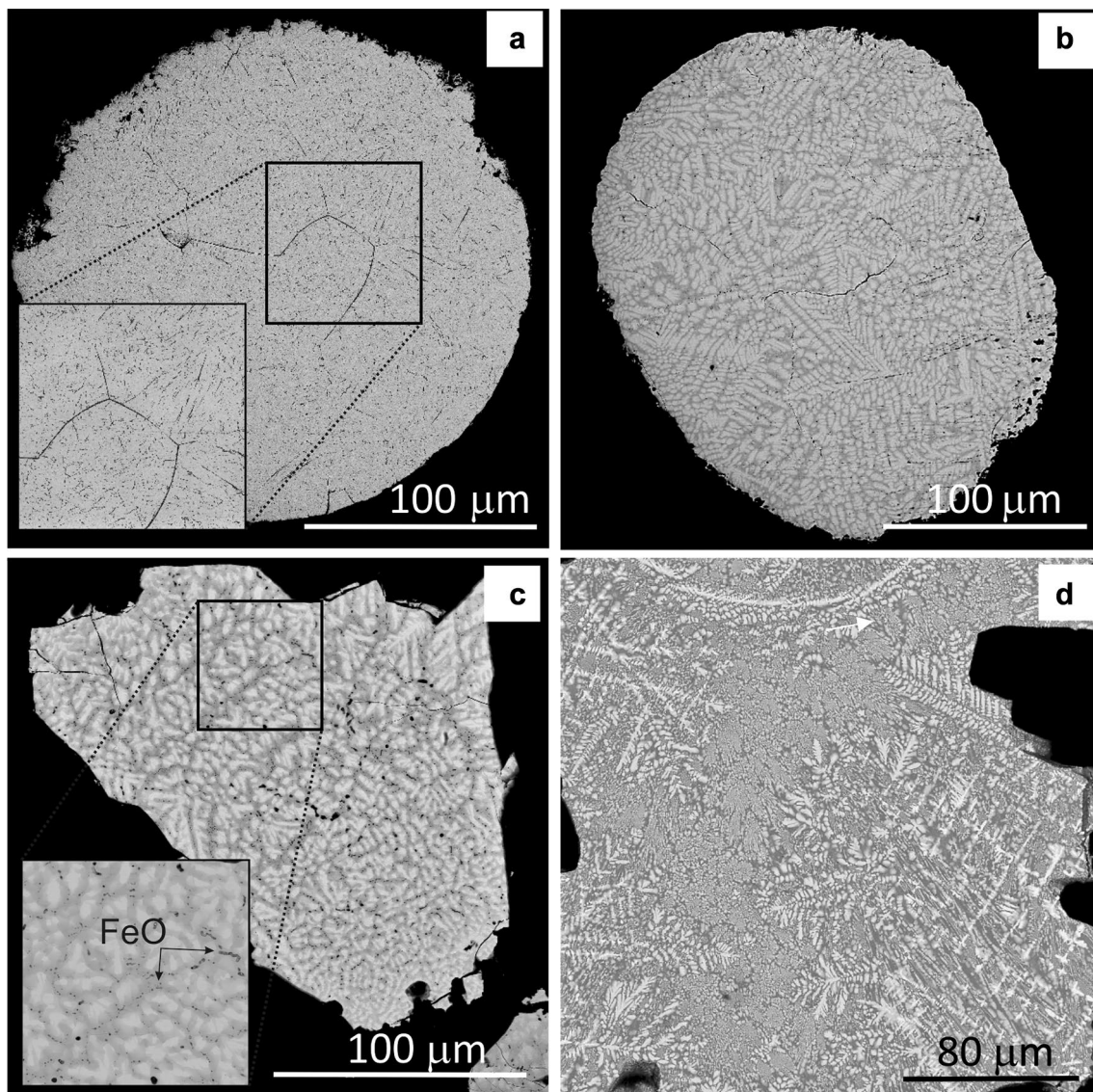

Fig. 2 SEM images of metal phases formed by interactions of an N-rich fluid with Fe^0 (**a, b**) and Fe$_3$C (**c, d**). **a**: γ-Fe, #1882_2_2, 6.3 GPa, 1300 °C (MMO); **b** quenched metal melt, #1882_2_1, 6.3 GPa, 1300 °C (MMO); **c** quenched metal melt, #1796_2_2, 7.8 GPa, 1400 °C (MMO); **d** quenched metal melt, #998_7_3, 7.8 GPa, 1400 °C (unbuffered). Inset enlarges textures from panels **a** and **c**

Analytical methods

Gas chromatography–mass spectrometry

The compositions of quenched fluids were analyzed by gas chromatography and mass spectrometry using a Thermo Scientific Focus GS/DSQ II Series Single Quadrupole MS analyzer (USA). After the run, the capsules were placed into a crush cell connected on-line to the gas chromatograph before the analytical column and heated at 120–130 °C for 90 min in a stream of carrier gas (99.9999% pure He); the gas mixture was extracted from the capsules by piercing. All gas released upon piercing after separation in the column flew into the MS detector. The mass spectra were obtained in the full scan mode, in the range 5–500 amu, at positive ion polarity. Hydrogen was not measured because the amount of quench fluid in the capsules was insufficient. Its determination in the gas mixture, along with all other compounds, would require separating the carrier gas flow and using a combination of sieve capillary columns with TCD or Valco helium ionization detectors.

In the GC–MS modification we applied, chromatography yielded specific retention times for each component, while mass spectrometry provided the mass spectra of each compound and information about its ionic and diagnostic fragments. The compounds were identified by combining both methods. The GC–MS data were interpreted for the identification of peaks and discrimination of components in overlapping peaks both using the AMDIS software (Automated Mass Spectral Deconvolution and Identification System), version 2.73, and manually, with background corrections based on mass spectra from the NIST 2017 and Wiley 11 libraries by means of NIST MS Search-2.3.

The TIC chromatogram in the GC–MS analysis is created by summing up the intensities of all mass spectral peaks (total ion signal) collected during a given scan (Budde 2001; Lebedev 2012). The greater the ion current, the higher the signal position, while the peak areas of specific ions are proportional to their amounts in the sample. Quantitative analysis (see (Budde 2001) for procedure details) is problematic because (i) ionization efficiency depends on the structures of compounds and (ii) the GC–MS discrimination of ions according to mass may be ambiguous (a signal from a certain number of ions with low m/z values may be stronger than that from the same number of ions with high m/z values). Mitigation approaches include adding some components to the charge or using interior/exterior standards and isotope dilution. These approaches, however, require either reloading samples or running preliminary experiments with gas mixtures of similar compositions. Neither is applicable to our case, in which the quenched multi-species fluid of an unknown composition is under some pressure in a tightly welded Pt capsule. After the capsule has been crushed, the fluid escapes with the He stream into the GC–MS spectrometer, and it cannot be reanalyzed. The complex compositions of the synthesized mixtures (more than 100 species), with strongly variable main components of H_2O, N_2, NH_3, alkanes and oxygenated HCs, rule out the calibration of the GC–MS analyzer. Based on the calibration we previously applied to a relatively simple N-poor reduced fluid (Sokol et al. 2017c), the analytical uncertainties for H_2O, NH_3, and CO_2, expressed as precision, were $< 10\%$ and even $< 5\%$ in most cases (in the range from 12.5 pptv to 12.5 ppbv). The uncertainty for C_1–C_4 alkanes was below 5%. For details of the GC–MS method, see (Sokol et al. 2017a).

The TIC peak areas are proportional to the number of molecules in the gas mixture. Therefore, the rel.% contents of fluid species, obtained by the normalization of the TIC chromatogram, correspond to a first approximation of their molar percentages. The wt.% C and N contents in the fluids were estimated by multiplying the rel.% contents of the fluid species (Supplementary Table 1) by their molecular weights, with their subsequent normalization to the sum (multiplied by 100). Thus, the estimated C and N concentrations in each species were summed over all species. The consistency of the obtained data was checked by mass balance calculations, assuming that atmospheric nitrogen was vanishing while melamine ($C_3H_6N_6$) was the only nitrogen host in the system. The mass of nitrogen in the fluid was calculated as the difference between its masses in the charge and in Fe–C–N phases. The mass of fluid synthesized in each run was estimated from the mass and GC–MS percentage of nitrogen it contained. The calculated fluid mass (minus water) was compared with that of starting melamine (the fluid-generating agent). As a result, strongly underestimated N concentrations were rejected for the fluids generated in three runs (1882_2_1, 998_7_3 and 1878_2_2). The C and N partition coefficients for the samples are accurate to 25 rel.%.

EDS and EMPA

At the end of the experiments, the recovered metal phases were cleaned and mounted in epoxy resin. After resin polymerization, the samples were polished under kerosene, without the use of water (final stage 1 μm Al_2O_3), and they were examined on a Tescan MYRA 3 LMU scanning electron microscope (SEM) and a Carl Zeiss Stemi 2000-C optical microscope. The metal-phase compositions were analyzed using a Tescan MYRA 3 LMU scanning electron microscope coupled with an INCA EDS 450 microanalysis system with an Oxford Instruments liquid nitrogen-free Large area EDS X-Max-80 Silicon Drift Detector. The instruments were operated at an accelerating voltage of 20 keV, a beam current of 1 nA, and a spot diameter of ~ 10 nm; the count time for spectra collection was 60 s. The EDS spectra were optimized

for quantification using the standard XPP procedure built into the INCA Energy 450 software.

The element abundances in the samples were determined by electron microprobe analysis (EMPA) using a Jeol JXA-8100 microanalyzer with an accelerating voltage of 15 kV, a beam current of 200 nA, and beam diameters of 1–2 μm for solids and 100 μm for quenched liquids, with gold sputtering at 10 nm. The results were checked against Fe_3N, Fe_3C, Fe, Pt and Fe_2O_3 standards. The measured intensities were converted to concentrations using the ZAF method. The C and N contents in solid phases were estimated to an accuracy of 5 rel.%, and Fe, Pt and O were accurate to 2 rel.%. The detection limit was 0.1 wt.% for C, N, and O at the applied analytical conditions. The errors in element contents were larger for quenched liquids because of their enclosed dendritic crystals. For this reason, the analytical quality was low even when using a beam diameter of 100 μm.

Elemental analysis

The EMPA data were complemented with quantitative analysis of N in solid phases by destructive elemental analysis, on a Carlo Erba-1106 CHN analyzer. The samples were weighed on a Sartorius CP2P balance. Aliquots of 0.5–2.0 mg were weighed in tin capsules and oxidized in a vertical reactor, in dynamic mode, at 1050 °C, in a He stream doped with 10 ml O_2 at the time of loading. After complete oxidation, the CO_2, H_2O and nitrogen oxides passed through a reduction zone, where hot copper removed excess oxygen and reduced nitrogen oxidized to N_2. The resulting N_2, CO_2, and H_2O mixture was separated in a *Porapak Q* column, and individual eluted gases were measured with a thermal conductivity detector to an accuracy of ± 0.3 wt% (Fadeeva et al. 2008). Unfortunately, it was impossible to estimate the carbon contents in the metal phase using this method because we failed to clean the outer surfaces of the samples with respect to graphite.

X-ray diffraction

The synthesized solid phases were identified by X-ray powder diffraction using a Stoe IPDS-2T diffractometer (MoKα radiation, graphite monochromator) in the Gandolfi mode. Two-dimensional X-ray patterns were radially integrated using the XArea software package. The diffraction profiles were processed in WinXPow (Stoe). For phase analysis, the database of PDF-4 Minerals (The Powder Diffraction File PDF-4 + 2006) was used. The concentrations of the identified phases were estimated using the Match! software based on the relative intensities of predicted and measured diffraction peaks, and their sum was normalized to 100%. The X-ray single-crystal diffraction (XRD) analysis of the synthesized phases was performed on a Stoe IPDS-2T

diffractometer (MoKα radiation, graphite monochromator). Diffraction data were collected with ω scans and processed with CrysAlis Pro (Oxford Diffraction 2005). A semi-empirical absorption correction was applied using the multi-scan technique. Crystal structures were determined with the *SHELX-97* package (Sheldrick 2008).

Results

The experiments with the Fe–C–O–H–N system were run at different Fe, C and N contents and fH_2 (Table 1): (i) low C and N insufficient for the formation of iron carbide and/or nitride; (ii) high C (excess graphite) and low N; and (iii) high C (excess graphite) and N (weight ratio Fe/N ≤ 14) sufficient for the formation of iron carbide and/or nitride. In all cases, the quenched samples with liquid or solid metal phases (Figs. 2, 3) contained fluids that could be analyzed by GC–MS. Note that fH_2 remained unbuffered in two runs, in which the system had fO_2 near IW buffered by the metal phase but was depleted in hydrogen because of leakage.

Solid and liquid phases

Two runs were performed at 6.3 GPa and 1300 °C, in the presence of Fe^0 and low concentrations of C and N, at MMO-buffered fH_2. In both cases, SiO_2 that insulated the metal from the Pt capsules converted to coesite, but no traces of its reactions with Fe^0 were observed. The fluid–metal interaction at the lowest C and N contents (weight ratio Fe/C = 71; Fe/N = 31) produced a phase free from melting signatures (Table 1; Fig. 2a), with 0.5 wt.% C and 0.9 wt.% N, as revealed by EMPA (Tables 2, 3). XRD analysis revealed high-temperature carbon–iron $Fe_{1.86}C_{0.14}$, which is austenite or γ-Fe (Table 4; Supplementary Fig. 1) called hereafter 'iron' for simplicity. When slightly greater amounts of C and N were present in the system (Fe/C = 51 and Fe/N = 22), the metal phase melted and produced typical textures upon quenching (Fig. 2b). This phase contained more C and N than solid iron: 2.3 wt.% C and 2.4 wt.% N (EMPA).

Iron carbide that interacted with fluid, in the case of graphite saturation and high N contents (Fe/N ranging from 7 to 14), at a pressure of 6.3 GPa and temperatures of 1200 and 1300 °C, converted to an N-rich phase. The hydrogen fugacity in those runs was buffered by the IW or MMO equilibria. The metal phase, which easily cleaves and is pale yellow on fracture, with perfectly homogeneous grains and no quench textures (Fig. 3), was identified as iron nitride by XRD analysis (see Table 4 for single-crystal XRD data). The compositions of the samples varied from $FeN_{0.22}$ to $FeN_{0.50}$ according to structure refinement results. Sample 1365_3_1 was composed of ε-Fe_3N with the space group $P6_322$ (Jacobs et al. 1995). The same ε-Fe_3N phase,
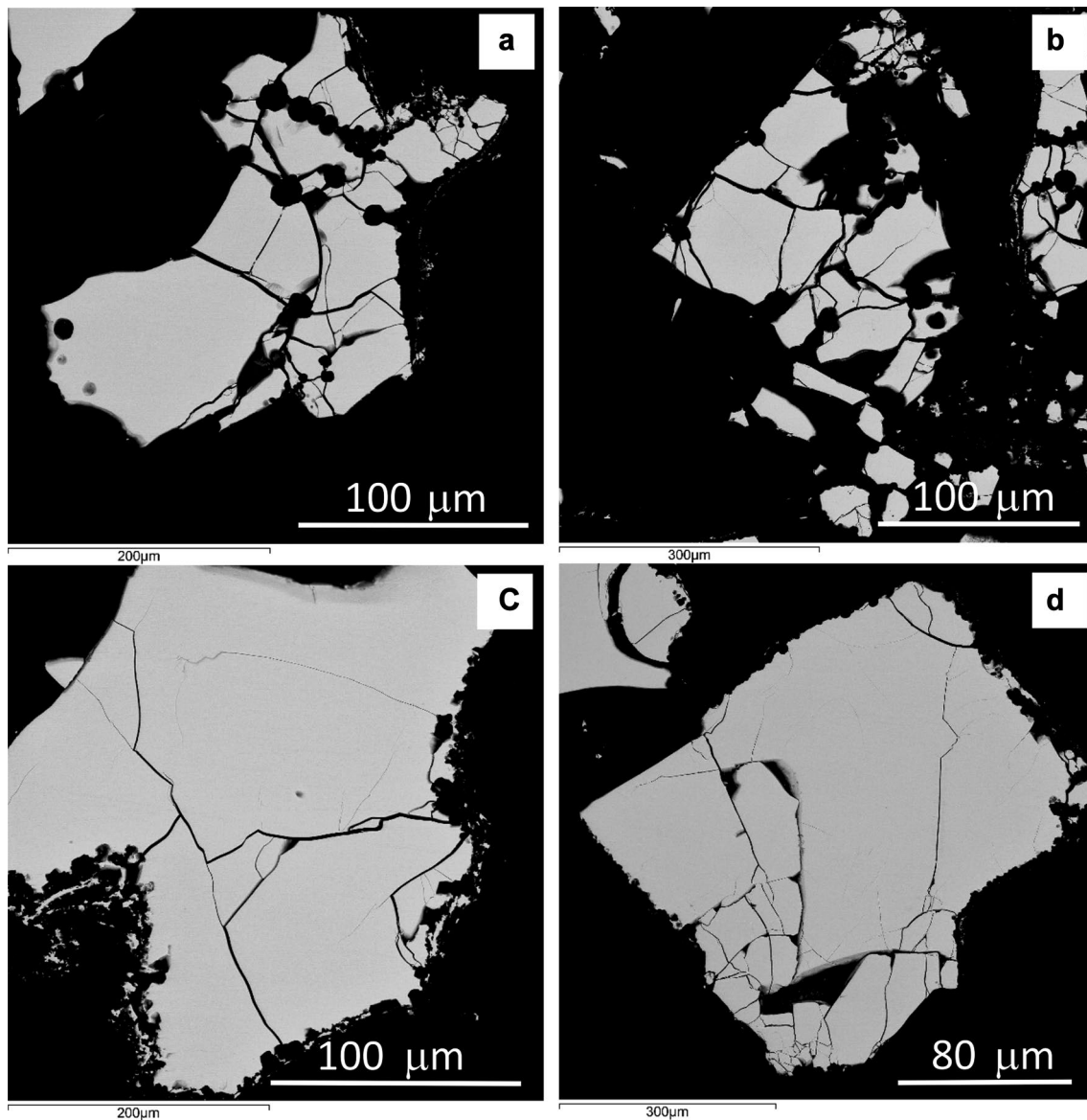
Fig. 3 SEM images of Fe$_3$N formed by interactions of an N-rich fluid with Fe$_3$C. **a** #1365_3_1, 6.3 GPa, 1200 °C (IW); **b** #1365_3_2, 6.3 GPa, 1200 °C (IW); **c** #1801_2_2, 6.3 GPa, 1300 °C (MMO); **d** #1778_2_1, 6.3 GPa, 1300 °C (MMO)

but with a higher symmetry of *P*6$_3$/*mmc* (Gajbhiye et al. 2008), was obtained in the other samples as well. Previously, we (Sokol et al. 2017c) studied iron nitride with the same unit-cell parameters in a Fe–Fe$_3$C–Fe$_3$N system at 7.8 GPa and 1350 °C. See Fig. 4 for the pfu volumes of iron nitride obtained in the Fe–C–O–H–N system and in the fluid-free Fe–Fe$_3$C–Fe$_3$N system discussed by Sokol et al. (2017c). Note that the approximating relationships $V_{fu}(N_x)$ have markedly different slopes (Fig. 5), which may be due to their different temperatures of iron nitride formation (Table 1). The amount of Pt in iron nitride from run 1801_2_2 (Table 2) was far too low to cause such a notable difference, i.e., 0.5 wt.% or 0.0015 pfu (the sum of cations being 1). The

phase that interacted with the fluid contained 3.8–7.0 wt.% N and 1.9–3.1 wt.% C, according to EMPA. Nitrogen varied from 4.1 to 6.7 wt.% and from 5.6 to 7.8 wt.% according to EDS and destructive elemental analysis, respectively (Table 3; Fig. 4).

Experiments at 7.8 GPa and 1400 °C were performed with Fe$_3$C and C$_3$H$_6$N$_6$, which provided bulk Fe/N ratios in samples ranging from 9 to 40. Note that fH$_2$ was buffered by MMO in the N-rich sample (Fe/N = 9) but was left unbuffered in two N-undersaturated samples (Table 1). In all cases, the interactions with the fluid led to the formation of a metal melt (Figs. 2c, d, 5a). N-rich melts synthesized at buffered fH$_2$ contained up to 5.2 wt.% N and as little as 2.4 wt.% C.

Table 2 Composition of metallic phases (EMPA, wt.%)

Run#	Phase	n	C	O	Fe	N	Pt	Total	$D_C^{Me/Fl}$	$D_N^{Me/Fl}$
1882_2_1	L	8	2.4 (2)	0.7 (1)	91.6 (4)	2.3 (1)	–	97.0	0.03[a]	1.13[a]
1882_2_2	Fe	7	0.5 (2)	0.5 (1)	98.5 (2)	0.9 (1)	–	100.5	0.02	0.05
1365_3_1	Fe_3N	8	1.9 (1)	0.4 (1)	91.1 (6)	7.0 (2)	–	100.5	0.05	0.18
1365_3_2	Fe_3N	8	2.0 (3)	0.4 (1)	91.0 (6)	6.9 (2)	–	100.3	0.11	0.39
1801_2_2	Fe_3N	8	2.3 (1)	0.5 (1)	91.5 (4)	3.8 (2)	0.5 (2)	98.7	0.11	0.34
1778_2_1	Fe_3N	8	3.1 (6)	0.7 (2)	91.0 (5)	5.1 (1)	–	99.9	–	–
1796_2_2	L	9	2.4 (2)	0.8 (1)	82 (1)	5.2 (2)	7 (1)	97.8	0.28	0.24
998_7_3	L	8	4.6 (2)	0.8 (2)	80.0 (4)	0.5 (1)	12.6 (3)	98.5	0.06[a]	0.16[a]
1878_2_2	L	6	3.9 (1)	0.56 (1)	83.5 (2)	1.4 (2)	10.2 (1)	99.6	0.06[a]	0.38[a]

$D_C^{Me/Fl}$ and $D_N^{Me/Fl}$ calculated with C and N concentrations in fluid from Table 5

n number of analyses. Numbers in parentheses show one sigma error, to last significant digit

[a] Mass balance calculations showed that the GC–MS-derived contents in the fluid phases were overestimated for carbon but underestimated for nitrogen

Table 3 Representative analyses of nitrogen content in metallic phases according to EDS and destructive elemental analysis (wt.%)

Run #	EDS	$D_N^{Me/Fl}$	Destructive elemental analysis	$D_N^{Me/Fl}$
1882_2_1	1.6	0.78[a]	–	–
1882_2_2	0.5	0.02	–	–
1365_3_1	6.7	0.17	7.6	0.192
1365_3_2	6.7	0.37	7.8	0.44
1801_2_2	4.1	0.36	5.6	0.40
1778_2_1	5.2	–	5.8	–
1796_2_2	4.9	0.23	–	–
998_7_3	0.5	0.16[a]	–	–
1878_2_2	1.7	0.46[a]	–	–

[a] Mass balance calculations showed that the GC–MS-derived N contents in the fluid phases were underestimated

At the same time, the melts generated from N-poor charges at unbuffered fH$_2$ were poor in N (0.5–1.4 wt.%, according to EMPA) and contained 3.9–4.6 wt.% C (Tables 2, 3; Fig. 5b). It is noteworthy that single-crystal XRD analysis revealed dendritic crystals of iron nitride in the quenched melt, as well as small soot-like carbon particles in some cases, even

in the runs with relatively low-N charges (Table 4). Note also that the metal melt became contaminated by 7 to 12.6 wt.% Pt despite the insulation of graphite.

Fluid phase

The compositions of the fluids synthesized in the Fe–C–O–H–N system under the applied experimental conditions were markedly different (Table 5; Figs. 6, 7, 8). The quenched fluid in equilibrium with solid iron, at C and N deficits in the system, mainly consisted of H_2O and NH_3, with minor N_2 and oxygenated HCs, as well as alkanes (mainly heavy species) (Fig. 6, 7a). Slightly higher concentrations of C and N allowed the formation of a fluid with an unusual composition, in addition to the melt: alcohols and esters were the main carbon species, and decanoic acid ethyl ester $C_{12}H_{24}O_2$ was predominant (Fig. 6, 8b, Supplementary Fig. 2). Note that HCs (alkanes, alcohols and esters, aldehydes, ketones, and carboxylic acids) are mostly heavy species (Fig. 8b). The experiments at 6.3 and 7.8 GPa and 1200–1400 °C yielded quenched fluids from N-rich charges with Fe_3C of more uniform compositions, with predominant

Table 4 Results of X-ray single-crystal analysis of $Fe(C,N)_n$

Sample	Unit-cell parameters, space group, formula unit number	Formula unit[a]
1365_3_1	$a = 4.7420(3)$, $c = 4.3912(4)$ Å, $V = 85.514(10)$ Å^3, $P6_322$, $Z = 6$	$FeN_{0.443(6)}$
1365_3_2	$a = 2.73522(18)$, $c = 4.3891(3)$ Å, $V = 28.438(3)$ Å^3, $P6_3/mmc$, $Z = 2$	$FeC_{0.50(3)}$
1801_2_2	$a = 2.69618(17)$, $c = 4.3627(3)$ Å, $V = 27.465(3)$ Å^3, $P6_3/mmc$, $Z = 2$	$FeN_{0.21(3)}$
1778_2_1	$a = 2.71394(18)$, $c = 4.3729(3)$ Å, $V = 27.894(3)$ Å^3, $P6_3/mmc$, $Z = 2$	$FeN_{0.22(4)}$
1796_2_2[b]	$a = 2.7224(12)$, $c = 4.374(2)$ Å, $V = 28.07(2)$ Å^3, $P6_3/mmc$, $Z = 2$	$FeN_{0.39(6)}$
1877_2_1[b]	$a = 3.8764(10)$ Å, $V = 58.25(2)$ Å^3, $Pm\bar{3}m$, $Z = 3$	$FeN_{1/4}$ (theor.)
1878_2_2[b]	$a = 2.6783(7)$, $c = 4.3668(11)$ Å, $V = 27.128(12)$ Å^3, $P6_3/mmc$, $Z = 2$	$FeN_{0.26(7)}$

[a] Phase composition according to structure refinement
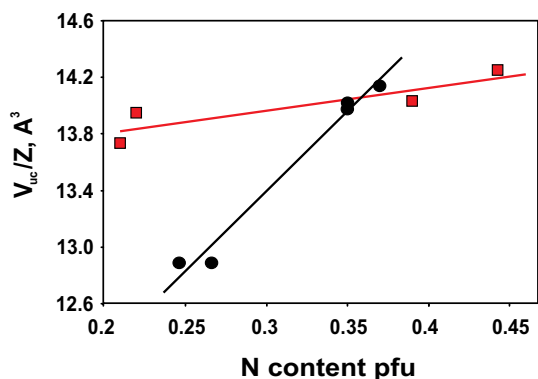
[b] Dendritic crystals from quench melt

Fig. 4 Volume of the ε-phase of iron nitride $Fe_3N_{\approx 1}$, per FeN_x formula unit vs. number of nitrogen atoms (x). Solid line is the linear polynomial obtained by approximation over all points. Red squares are new data; circles are data from Sokol et al. (2017a)

H_2O and NH_3 and lesser amounts of light alkanes and N_2 (Figs. 7b, 8a).

The graphite-saturated charges with Fe_3C and low nitrogen contents in the experiments at 7.8 GPa and 1400 °C, at unbuffered fH_2, yielded a fluid phase with light alkanes and N_2 ($NH_3/N_2 < 0.1$) as the principal nitrogen host (Fig. 8c, d). Figure 6 shows an unusual TIC spectrum of the fluid from run 1878_2_2 containing abundant acetic acid (Supplementary Fig. 2), elevated contents of other carboxylic acids, and alcohols, aldehydes, and ketones (Table 5; Fig. 8c). Note that this experiment led to the formation of diverse nitrogen heterocycles and linear nitriles, with their total amount exceeding that of ammonia. The fluid with higher N_2 from run 998_7_3 contained still greater amounts of O-bearing HCs, with a peak at tetradecanoic acid $C_{14}H_{28}O_2$ (Fig. 8d). The relatively low water contents in the fluid phase can be attributed to the formation of oxygenated HCs and hydrogen leakage.

Fluid/metal partitioning of C and N

The contents of nitrogen in the metal phase produced by the interactions with fluids increased with increasing bulk nitrogen and decreasing Fe/N ratios in the charges in both the C-unsaturated Fe^0-fluid and graphite-saturated Fe_3C–fluid systems (Fig. 5a, b). In the latter case, the initial iron carbide was converted into iron nitride by the reaction:

$$Fe_3C + N_{Fl} \rightarrow Fe_3N + C_{Gr,Dm,} \tag{1}$$
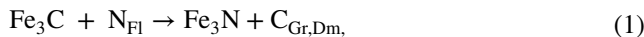
at 1200–1300 °C, though the bulk weight Fe/N ratio was as low as 12 (Tables 1, 2, 3; Fig. 5a), while the excess carbon was released as graphite. In contrast, the same interaction at 1400 °C led to the formation of an N-rich melt instead of iron nitride. No diamond formed in those runs because its nucleation and growth in N-rich systems would normally require higher temperatures (Borzdov et al. 2002; Palyanov et al. 2010).

The key question is whether C and N were repartitioned between the metal phase and the fluid during quenching. Iron in the C- and N-unsaturated run formed a high-temperature C- and N-bearing solid solution (γ- Fe) that was stable during quenching (Supplementary Fig. 1). The quenching of the metal melt produced an aggregate of dendritic crystals, which consisted of iron nitride in N-rich samples (Table 4). Iron nitride was likewise stable during quenching. Fluid inclusions were found in none of the quench metal phases, including the melt (Figs. 2, 3). The presence of small soot-like carbon particles (Fig. 2c) dissolved in the melt at the applied run conditions was automatically taken into account using a defocused probe. The resulting contents of C and N
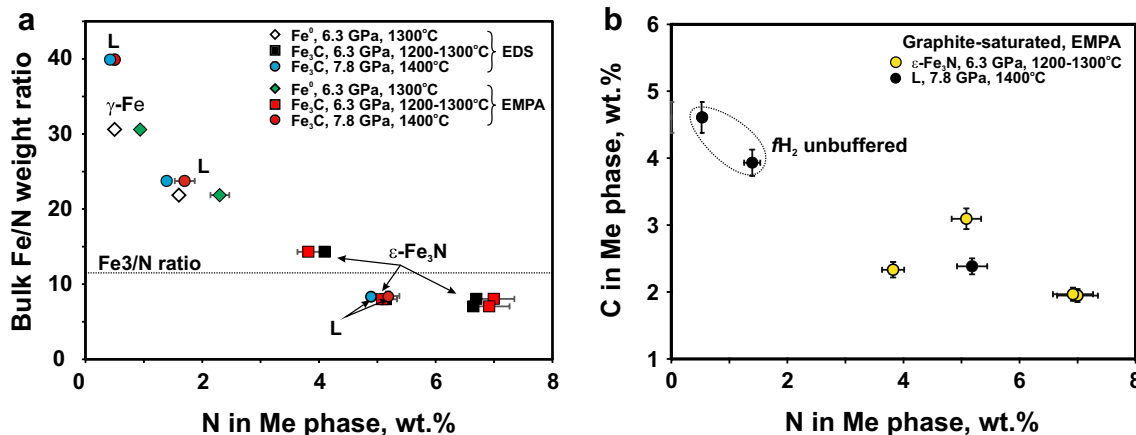

Fig. 5 Composition of metal phase produced by interactions of an N-rich fluid with Fe^0 and Fe_3C according to EDS and EMPA data. **a** nitrogen content as a function of bulk weight ratio Fe/N in the charge;

b variations of carbon and nitrogen in metal phases obtained in the graphite-saturated 'N-rich fluid–Fe_3C' system

Table 5 Composition of quenched fluid formed in the Fe–C–O–H–N system (rel.%)

| Run #	An	En	Ar	OH	CHO	CO	COOH	N_2	CH_3N	H_3N	H_2O	CO_2	C	N
1882_2_1	11.7	0.4	0.4	33.8	9.0	4.3	2.2	6.6	0.2	11.6	18.1	1.7	71.8[a]	2.0[a]
1882_2_2	2.1	0.3	0.4	0.6	2.4	0.5	0.6	3.9	0.1	34.7	54.0	0.3	32.0	19.8
1365_3_1	16.7	<0.1	<0.1	0.2	<0.1	<0.1	<0.1	7.7	0.5	63.9	10.3	0.7	35.1	39.7
1365_3_2	1.8	<0.1	<0.1	0.2	<0.1	<0.1	<0.1	2.7	<0.1	23.7	71.6	0.1	17.9	17.9
1801_2_2	14.8	<0.1	<0.1	0.3	<0.1	<0.1	<0.1	1.8	0.2	11.7	71.2	<0.1	20.2	11.3
1796_2_2	2.4	<0.1	<0.1	0.5	<0.1	0.2	<0.1	4.6	0.4	22.0	68.3	1.6	8.6	21.6
998_7_3	7.5	<0.1	<0.1	6.8	9.1	2.8	45.4	15.2	<0.1	<0.1	0.4	0.3	73.9[a]	3.2[a]
1878_2_2	20.4	3.1	1.8	5.6	15.4	11.0	30.0	9.4	0.2	0.9	2.0	0.1	68.7[a]	3.7[a]

An alkanes, *En* olefins, *Ar* arenes, *OH* alcohols, esters and ethers, *CHO* aldehydes, *CO* ketones, *COOH* carboxylic acid; furans in all samples ≤ 0.1 rel.%

Capsules became unsealed during GC–MS analysis after run # 1778_2_1

C and N are carbon and nitrogen concentrations in fluid (wt.%), calculated as rel.% × molecular weight of species normalized to total and multiplied by 100

[a]Mass balance calculations showed that the GC–MS-derived contents in the fluid phases were overestimated for carbon but underestimated for nitrogen

Fig. 6 Fragments of TIC chromatograms for quench fluids from C- and N-unsaturated runs (#1882_2_1, 1882_2_2) and N-unsaturated but graphite-saturated run (#1878_2_2). 1 = nitrogen, methane and carbon dioxide; 2 = ammonia; 3 = water; 4 = n-butane; 5 = furfural; 6 = nonanoic acid; 7 = decanoic acid, ethyl ester; 8 = tetradecanal; 9 = acetic acid; 10 = (E)-3-penten-2-one; 11 = butanoic acid; 12 = benzaldehyde; 13 = acetophenone; 14 = nonanal; 15 = decanal
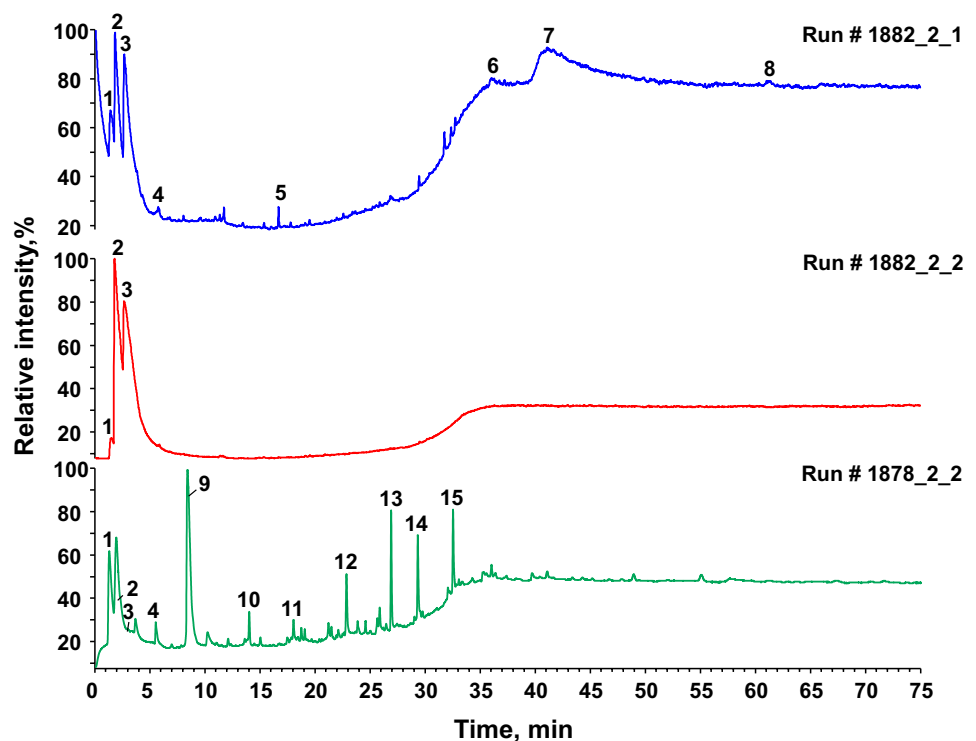
in the metal phases agreed well with their solubility limit in solid iron, Fe_3N, and melt, which was also observed in the fluid-free system $Fe–Fe_3C–Fe_3N$ (Sokol et al. 2017a). Thus, quenching did not lead to the notable metal/fluid partitioning of C and N.

Effective partition coefficients were estimated from the C and N concentrations in the metal phase and fluid (Tables 2, 5, Fig. 9). The obtained $D_C^{Me/Fl}$ and $D_N^{Me/Fl}$ values (Tables 2, 5; Fig. 10) depended on both the metal and fluid compositions, which were controlled by the charge composition and fH_2. However, $D_C^{Me/Fl}$ was much lower than $D_N^{Me/Fl}$ in all cases. Similar values of the coefficients were obtained for sample 1796_2_2, in which the fluid was in equilibrium with the metal melt contaminated with 7 wt.% Pt at relatively low Fe/N = 8.6 in carbon-saturated runs. In the two other runs, the presence of Pt in melts (up to 12.6 wt.%) neither changed the relative values of the C and
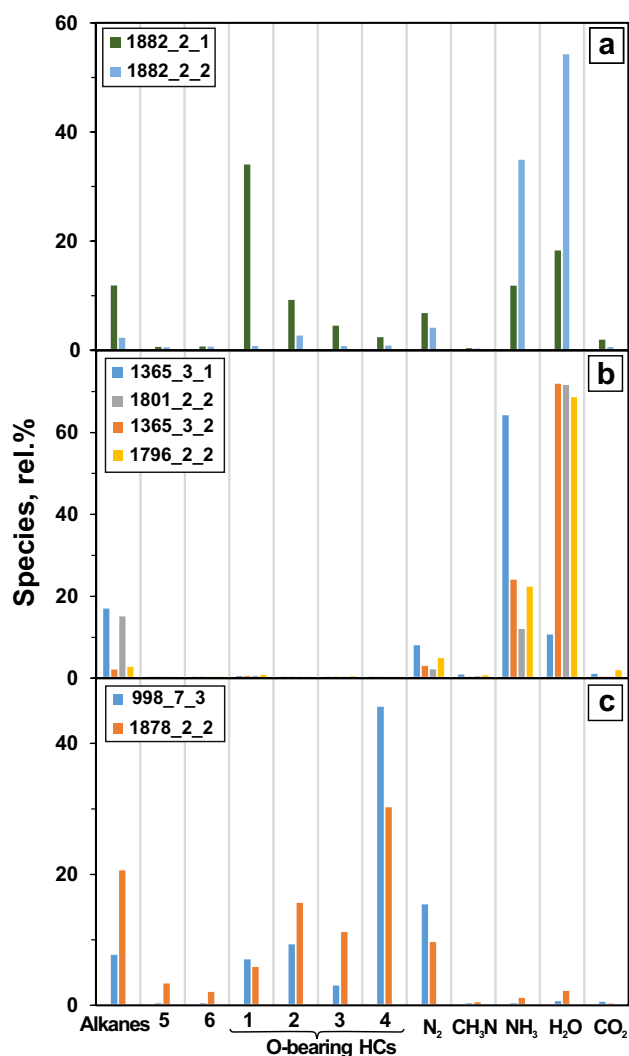
Fig. 7 Composition of quench fluid obtained in the Fe–C–O–H–N system. **a** 6.3 GPa, 1300 °C (MMO) C- and N-unsaturated Me phase (solid iron, melt); **b** 6.3 GPa, 1200–1300 °C (IW, MMO) C- and N-saturated metal phase (ε-Fe₃N, melt); **c** 7.8 GPa, 1400 °C (unbuffered), C-saturated and N-unsaturated metal melt. 1 = alcohols, esters and ethers; 2 = aldehydes; 3 = ketones; 4 = carboxylic acid; 5 = olefins; 6 = arenes

N partition coefficients (Table 2) nor greatly influenced the solubility of nitrogen and carbon.

Among all metal phases, solid iron stored the lowest amounts of C and N equilibrated with the fluid containing approximately 32 wt.% C and 20 wt.% N, and their partition coefficients did not exceed 0.02 and 0.05, respectively. As a rule, the metal/fluid partitioning of carbon was the lowest when the fluid was rich in carbon due to the presence of abundant heavy HCs, for instance, in samples 1882_2_2 and 1878_2_2 (Tables 2, 5). Interestingly, fH_2, which controlled the stability of nitrogen species at invariable fO_2, did not influence the metal/fluid partitioning of nitrogen. The $D_N^{Me/Fl}$ coefficient was highest in the system where the melt was
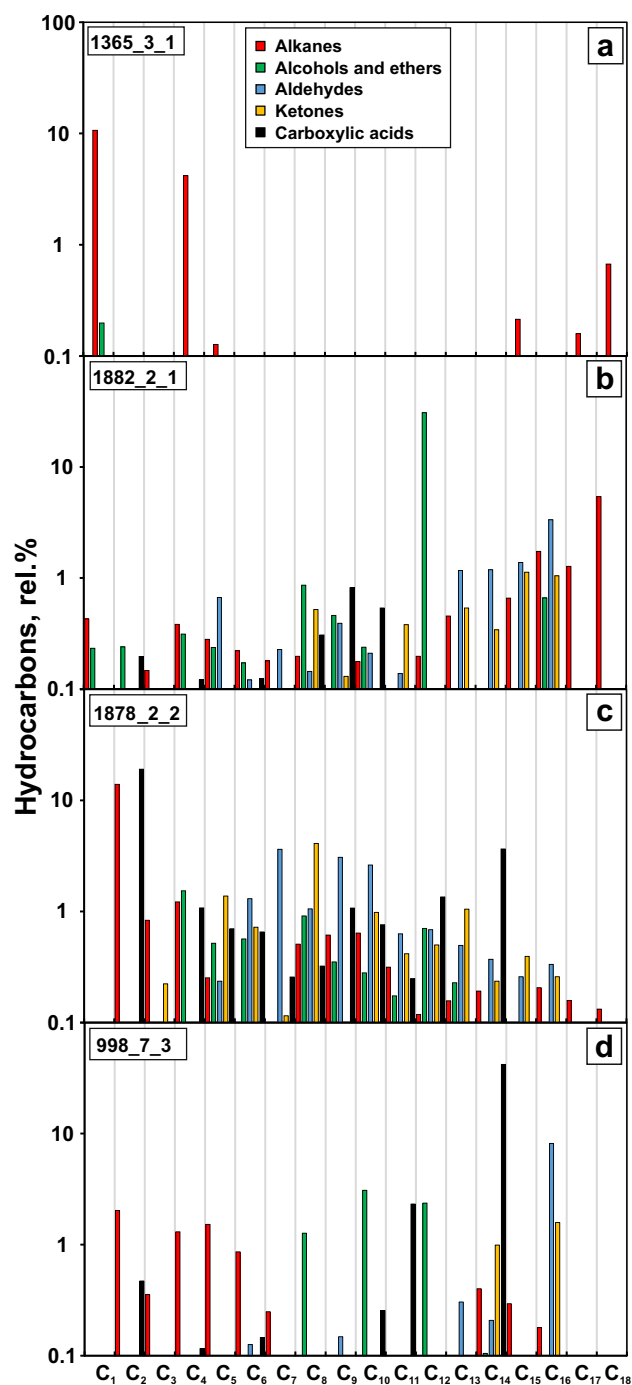

Fig. 8 Hydrocarbon speciation in quenched fluids. **a** C- and N-saturated run (#1365_3_1); **b** C- and N-unsaturated run (#1882_2_1); **c, d** C-saturated and N-unsaturated runs (#1878_2_2, 998_7_3)

equilibrated with a fluid rich in oxygenated HCs but only had 2 wt.% N. Note that the C and N partition coefficients determined based on EDS and destructive elemental analysis were similar to those determined based on EMPA (Table 3).

The quality of this estimation was assessed by mass balance calculations (Fig. 9, see the Methods section), and the
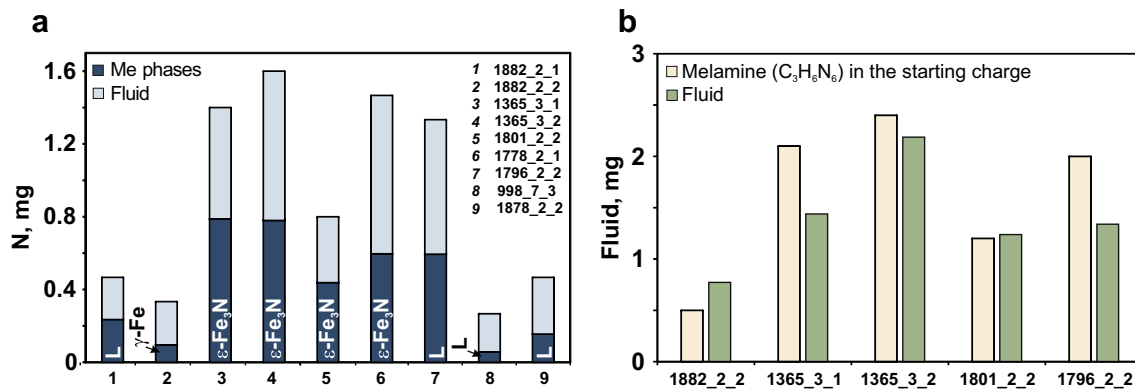
Fig. 9 Mass balance calculation results. **a** Mass of nitrogen in metal and fluid phases based on starting compositions and EMPA data (Tables 1, 2); **b** Mass of melamine (main fluid-generating component) in the starting charge compared to that of fluid calculated from mass (Fig. 9a) and GC–MS percentage of N in the fluid (see the *Methods* section)
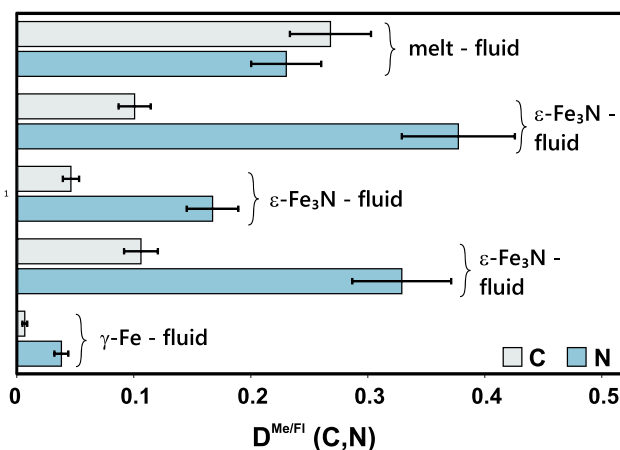

Fig. 10 Tentative metal/fluid partition coefficients of C (green bars) and N (blue bars) at 6.3–7.8 GPa and 1200–1400 °C with different C and N contents in the system

data of three runs were rejected (1882_2_1, 998_7_3 and 1878_2_2). These calculations showed that the GC–MS-derived contents in the fluid phases were overestimated for carbon but underestimated for nitrogen. Note that the fluid phases obtained in all of these runs contained high concentrations of heavy hydrocarbons (Table 5).

Discussion

Effect of the metal phase and fH$_2$ on fluid composition

The fluid composition in a C- and N-saturated metal–fluid system at fH$_2$ buffered by the MMO and IW equilibria (Tables 2, 5; Figs. 7b, 8a) experiences no specific influence of the metal phase (Fe$_3$N or metal melt). It contains abundant

water, ammonia, and alkanes but lesser amounts of molecular nitrogen and is compositionally similar to the N-rich fluids from the C–O–H–N system we studied at the same P–T conditions (Sokol et al. 2017a). The presence of HCs in equilibrium with a C-saturated metal melt is supported by the discovery of methane in fluid inclusions from diamond in experiments (Tomilenko et al. 1998; Palyanov et al. 2012) and in natural mantle-derived (including sublithospheric) diamonds (Smith et al. 2016). Fluids with more complex compositions form in equilibrium with solid iron and, to a greater degree, with C- and N-undersaturated metal melts at buffered fH$_2$ (Tables 2, 3, 4, 5; Figs. 5, 7a, 8b). They contain abundant oxygenated HCs but low amounts of alkanes and water. Alcohols and esters are the main carbon species (34 rel.%), while water does not exceed 20 rel.%. Note that such fluids show trends of increasing species concentrations with increasing molecular weight from C$_1$ to C$_{18}$; the highest concentrations are observed for alkanes, alcohols and esters, aldehydes, ketones and carboxylic acids, namely, the C$_{18}$, C$_{12}$, C$_{16}$, C$_{15}$ and C$_9$ species, respectively (Fig. 8b). Such a composition is similar to the mixtures of alkanes, alkenes, and oxygenated HCs typically obtained by Fischer–Tropsch-type reaction hydrothermal experiments (McCollom et al. 1999; Davis 2009). Note that the fH$_2$ buffer worked well in the experiments, judging by the presence of an oxide phase (MoO$_2$) on the inner walls of the outer Mo capsule and by the marked enrichment of NH$_3$ relative to N$_2$ in the inner capsule.

A particular fluid composition was also obtained in runs without external fH$_2$ buffering. As noted above, fO$_2$ in the fluid was maintained around the IW equilibrium based on the metal melt composition and presence of FeO grains in the samples. Nevertheless, N$_2$ was the main fluid component: NH$_3$/N$_2$ < 0.1 (Table 5). Thus, ammonia is stable in the fluid phase only at low fO$_2$ and relatively high fH$_2$. Previously, we (Sokol et al. 2017a) did not study the composition

of N-rich C–O–H–N fluids with such a combination of $f\text{O}_2$ and $f\text{H}_2$, and we thus underestimated the importance of high $f\text{H}_2$ for ammonia stabilization. The species composition of hydrocarbons in these fluids is also unusual (Figs. 7c, 8c, d): ethane is the predominant alkane, while methane occurs in trace amounts, and aldehydes reach relatively high contents among oxygenated HCs, but the contents of ketones and especially carboxylic acids are still higher. The fluid from run 1878_2_2 contained more acetic acid than ethane (Fig. 8c), while tetradecanoic acid was predominant in that from 998_7_3. Note that the patterns of HC species distributed according to weight look different from those in 1882_2_1: either with a local maximum (Fig. 8c) or without a prominent trend (Fig. 8d). The contents of H_2O are very low, possibly because it was spent on the formation of oxygenated HCs, mainly carboxylic acids. The fluid from run 998_7_3 contained substantial amounts of bound nitrogen, presumably in the form of nitriles and heterocycles.

Thus, O-bearing HCs are stable in equilibrium with the metal phase at 6.3–7.8 GPa and 1300–1400 °C, in a large range of $f\text{H}_2$, and they may be the main carbon species in the fluid phase equilibrated with metal melt. The decrease of $f\text{H}_2$ from MMO to the values common in unbuffered samples at constant $f\text{O}_2$ leads to the prevalence of carboxylic acids (Fig. 8c, d) in the fluid phase instead of carbonyl compounds and esters (Fig. 8b); both heavy and light species can be predominant. The fluid that equilibrated with the C- and N-saturated metal phase (Fe_3N, melt) is compositionally similar to those obtained in the C–O–H–N system under similar P–T–$f\text{O}_2$–$f\text{H}_2$ conditions (Sokol et al. 2017a). The stability of ammonia in the metal–fluid system also depends on $f\text{H}_2$: NH_3 converts to N_2 at $f\text{O}_2$ near IW and $f\text{H}_2$ decreases as a result of hydrogen leakage.

Affinities of C and N for the metal phase, compared

Hitherto, the affinities of carbon and nitrogen for iron have commonly been compared based on their solubilities in metal and silicate melts. Carbon was reported (Dasgupta et al. 2013a) to behave as a metal-loving element at 1–5 GPa and 1600–2100 °C, yielding experimental $D_\text{C}^\text{Me/Sil}$ values between ~4750 and ≥ 150, increasing with pressure but decreasing with temperature and the depolymerization of silicate melts (tholeiitic basalt, alkali basalt, komatiite and fertile peridotite). Note that in the experiments of Dasgupta et al. (2013a), $f\text{O}_2$ was constrained by the coexistence of Fe-rich metal and mafic–ultramafic silicate melts between ~1.5 and 1.9 log units below IW. The $D_\text{C}^\text{Me/Sil}$ values obtained in a recent study of C partitioning between metal and silicate liquids (MORB melt) at 1.5–8.0 GPa, 1600–2200 °C, and IW-5.3 log units (Li et al. 2016b) reached ~1200 at an oxygen fugacity of IW-0.4 and 0.1 wt.% H_2O in the melt but were far lower (~100) at IW-3.7 log units and 1.0 wt.% H_2O.

The metal/silicate melt partition coefficient of nitrogen was reported (Roskosz et al. 2013) to change from almost 10^4 at ambient pressure to just 10–20 above 1 GPa in experiments that studied nitrogen solubility in a mixture of a molten CI-chondrite model composition and a (Fe, Ni) metal alloy liquid at 5–18 GPa and ~2100–2570 °C. The experiments of Li et al. (2016a) performed at 1.5–7.0 GPa and 1600–1800 °C yielded partition coefficients of nitrogen between coexisting liquid Fe-rich metal and silicate melt (MORB) ranging from 1 to 150, with the highest value occurring at $f\text{O}_2$ near IW. Such a low $D_\text{N}^\text{Me/Sil}$ value at a high pressure is due to the high N solubility in the silicate melt (0.5–0.7 wt.%) maintained by the stability of reduced nitrogen species (N_3^- and N–H complex) in silicate melts at low $f\text{O}_2$ (Libourel et al. 2003; Mysen et al. 2008; Kadik et al. 2011) and is consistent with published results (Roskosz et al. 2006; Mysen et al. 2008; Mysen and Fogel 2010; Kadik et al. 2011, 2013). Li et al. (2015) attributed the elevated nitrogen contents in silicate melts to the dissolution of NH_3 based on micro-Raman spectroscopy evidence.

The available data suggest that carbon has a higher affinity for the metal phase than nitrogen in the metal–silicate system at mantle pressures and super-liquidus temperatures ~2100 °C, at which the metal melt presumably separated from the silicate mantle and moved into the core after the formation of the magma ocean on the early Earth (Abe 1997; Solomatov 2000; Dasgupta 2013). The concurrent partitioning behavior of C and N in metal–silicate systems was recently studied by Dalou et al. (2017). As they reported, the $D_\text{N}^\text{Me/Sil}/D_\text{C}^\text{Me/Sil}$ ratios in the system of the metal alloy Fe–N–C plus a silicate melt (either terrestrial or martian basalts) decrease from 0.1 to 0.01 when $f\text{O}_2$ decreases from 0.5 to 2.5 log units below IW in experiments at 1.2–3 GPa and 1400–1600 °C.

Our experiments reproduced the upper mantle P–T conditions at depths from 200 to 250 km, with a heat flux of ~ 40 mW/m^2 (Fig. 1). At these conditions ($T = 1250$–1400 °C, $P = 6.3$–7.8 GPa) and $f\text{O}_2$ near IW, the peridotite–C–O–H system is below the solidus (Taylor and Green 1988; Litasov et al. 2014). In the absence of a silicate melt, the solubility of carbon in upper mantle silicates increases as a function of pressure to a maximum of ~ 12 ppm by weight in olivine at 11 GPa, but it shows no clear dependence on temperature, $f\text{O}_2$ or iron content (Shcheka et al. 2006). The solubility of nitrogen in the main peridotitic minerals of olivine, orthopyroxene, clinopyroxene, and garnet was estimated (Li et al. 2013) as 3.8, 208, 208, and 60 ppm, respectively, in experiments at 2.0 GPa, 1300 °C, IW-buffered $f\text{O}_2$, and with an NH_3-enriched fluid phase added to the starting material for the nitrogen saturation of silicates. At higher $f\text{O}_2$, around the NNO equilibrium, the fluid changed from an NH_3-rich to an N_2-rich composition (Li and Keppler 2014; Sokol et al. 2017a), and the solubility of nitrogen in silicates became ten

times lower (Li et al. 2013). Thus, the studied Fe–C–O–H–N system is a first-approximation model of the interactions between fluid and metal-saturated peridotite in the absence of stable silicate melts. The metal/fluid partitioning of C and N during such interactions should control the mobility of volatiles. The partition coefficients $D_C^{Me/Fl}$ and $D_N^{Me/Fl}$ we obtained do not contradict but rather complement the previously reported $D_N^{Me/Sil}$ and $D_C^{Me/Sil}$ values (Dasgupta et al. 2013a; Roskosz et al. 2013; Li et al. 2016a, b; Dalou et al. 2017). The $D_C^{Me/Fl}$ and $D_N^{Me/Fl}$ and $D_N^{Me/Sil}$ and $D_C^{Me/Sil}$ pairs refer to the partitioning of C and N between the metal and fluid phases, and between the metal and the silicate liquid, respectively, at different temperatures. The metal and fluid phases are the principal C and N hosts in the Fe^0-saturated mantle below the solidus of silicate rocks, but most C and N reside in the metal and silicate melts at super-liquidus temperatures when the fluid becomes completely dissolved in the silicate melt and does not exist as a stable phase. The difference between these coefficients is primarily due to the fact that the solubility of C and N in the fluid phase is about ten times greater than that in a silicate melt (Table 5) (Dasgupta et al. 2013a; Roskosz et al. 2013; Li et al. 2016a, b; Dalou et al. 2017). Furthermore, N becomes much more soluble in Fe-rich metal at graphite-saturated conditions as the pressure increases from 1.5 to 8.0 GPa, and nitrogen just excludes carbon from it, as shown by the comparison of our results to those of Li et al. (2016a, b) and Dalou et al. (2017).

In the case of graphite saturation, the N-rich fluid reacts with Fe$_3$C to form Fe$_3$N (an N-rich melt) by reaction (1), while excess carbon precipitates from the metal phase. Note that iron nitride formed at 6.3 GPa, 1300 °C and buffered fH$_2$ and was stable in equilibrium with H$_2$O-rich fluids containing only 11 wt.% N, mainly as NH$_3$ (Table 5). Therefore, nitrogen obviously has a greater affinity for iron than carbon. This relation also holds when Fe^0 reacts with fluid in a C- and N-depleted system: $D_C^{Me/Fl}$ varying between 0.02 (solid iron) and 0.03 (liquid) are notably lower than $D_N^{Me/Fl}$ values, which range from 0.05 to 1.1, respectively (Table 2; Fig. 10). Carbon and nitrogen dissolved in iron and melt have equal concentrations, but the equilibrium fluid contains much more C (Tables 2, 5), except for one case in which the $D_C^{Me/Fl}$ and $D_N^{Me/Fl}$ values are similar. Note that the obtained coefficients are tentative and only represent the Me/Fl partitioning trends of C and N.

The low solubility of nitrogen in iron carbide and the high solubility of carbon in nitride may be responsible for the replacement of Fe$_3$C by Fe$_3$N at excess C and N in the system. The solubility of nitrogen in cementite (Fe$_3$C), which has a structure consisting of approximately hexagonal close-packed iron atoms and carbons occupying a trigonal prismatic site, does not exceed 0.5 wt.% in the case of its equilibrium with N-rich melt at 7.8 GPa and 1350 °C. The dissolution of nitrogen in cementite makes its pfu volume

7–11% greater than that of N-free Fe$_3$C (Sokol et al. 2017c). This low solubility agrees with the estimates obtained under ambient pressure (Kagawa and Okamoto 1981). At 1 atm, ε-Fe$_3$N can accommodate a large amount of carbon within the octahedral interstices of its close-packed structure, thus leading to the formation of iron carbonitride ε-Fe$_3$(C/N) (Jack 1948). According to our data (Sokol et al. 2017c), the solubility of C in ε-Fe$_3$N reaches 2.5 wt.% at 7.8 GPa and 1350 °C. The stability of nickel nitrides until ~ 1350 °C at 1 atm (Guillermet and Frisk 1991) suggests that the minor Ni increase in the metal phase equilibrated with fluids should not greatly affect the solubility of nitrogen in the solid Fe–Ni alloy and melt.

The metal melts that formed in the N-poor Fe–C–O–H–N system at carbon-saturated or unsaturated conditions contained elevated C or equal concentrations of C and N, respectively (Tables 2, 3; Fig. 5b). Even at Fe/N > 20 in the charge, the carbon contents in the melt varied from 2.4 to 4.6 wt.% and failed to reach their solubility limit in the Fe-graphite system of ~ 6 wt.% at the applied experimental conditions (Lord et al. 2009; Dasgupta et al. 2013). Thus, the solubility of carbon in the Fe^0 melt becomes notably lower at higher nitrogen contents. Extrapolating the obtained relationships to the *P–T* conditions of metal phase segregation in the magma ocean, one may expect that nitrogen will easily dissolve in the metal melt even with excess carbon, whereby the latter will become less soluble. Then, the slightly lower amounts of C and some amounts of N dissolved in the metal melt may have been mobilized into the core. This behavior of nitrogen is consistent with the inference of Marty (2012) and Roskosz et al. (2013) that "lost nitrogen" was captured by metal melt and then mobilized into the core. Carbon remaining in the mantle may have stayed in the silicate matrix as diamond/graphite. The idea that nitrogen can expel carbon from the metal melt may also explain why the present mantle contains more carbon than it would have under quasi-equilibrium metal–silicate partitioning, with $D_C^{Me/Fl}$ values typical of an N-free system (Dasgupta et al. 2013).

Effect on the deep carbon and nitrogen cycles

The estimated values of $D_C^{Me/Fl}$ and $D_N^{Me/Fl}$ depend on both the metal phase composition and stable HC species in the fluid. Therefore, the effect of metal–fluid interactions on the deep carbon and nitrogen cycles can be evaluated based on the composition of the metal phase in the upper mantle. Depleted and enriched mantle domains contain different amounts of dissolved C and N, typically 20 and 1 ppm in the former and 250 and ~100 ppm in the latter, respectively (Dasgupta and Hirschmann 2010; Marty 2012; Li and Keppler 2014). Proceeding from the phase relations for the Fe–Fe$_3$C–Fe$_3$N system, we (Sokol et al. 2017c) inferred that the dissolution of these volatiles in the

metal phase, which makes up 0.1 wt.% of rocks at a depth of ~250 km at the adiabatic temperature T_p=1300 °C (Hasterok and Chapman 2011), would lead to the formation of a metal melt coexisting with γ-Fe in depleted mantle and with Fe_3C in enriched mantle. The concentration of N in the metal phase can be evaluated using data obtained from inclusions in sublithospheric diamond. On the one hand, diamonds contain inclusions of N-rich carbonitrides and iron nitrides (Kaminsky and Wirth 2011, 2017), indicating the N saturation of the metal melt that was the growth medium for diamond. On the other hand, many large sublithospheric diamonds with metal-phase inclusions belong to type IIa, with < 10 ppm N (Smith et al. 2016). The available samples of sublithospheric diamonds contain 56 ppm N on average (Smith and Kopylova 2014), while the effective N partitioning between diamond and a C- and N-saturated metal melt is as low as 0.005–0.013 (Borzdov et al. 2002; Smith and Kopylova 2014). If sublithospheric diamonds crystallized from a metal melt, the latter would be saturated with carbon and contain as little as 0.4–1 at.% (0.1–0.3 wt.%) N, or still less in the case of type IIa diamond.

At $D_C^{Me/Fl}$ and $D_N^{Me/Fl}$ below 0.05 for solid iron, the fluid that forms in depleted mantle at high hydrogen fugacity, in equilibrium with solid metal, contains ~30 wt.% C (as O-bearing HCs and alkanes) and ~20 wt.% N (mainly as NH_3). This will provide C and N mobility even in reduced mantle domains with low volatile contents. The fluid phase that equilibrates with carbon-saturated melts, which are potential growth media for sublithospheric diamonds, may contain up to ~70 wt.% C (as O-bearing HCs and alkanes) and ~3–4 wt.% N (as N_2), at low hydrogen fugacity, according to our estimates. Under these conditions, $D_C^{Me/Fl} < D_N^{Me/Fl}$, which provides the selective binding of nitrogen in the melt and the high mobility of carbon in HC-rich fluid. These interactions may produce (i) iron nitride equilibrated with fluid in enriched mantle domains at the adiabatic temperature $T_p = 1300$ °C and high fH_2, or (ii) a C- and N-saturated melt at a slightly higher temperature of 1400 °C. Fluids in equilibrium with these phases may consist mainly of water, light alkanes, and ammonia and bear low percentages of O-bearing HCs. In this case, fluid–melt interactions will result in the greater mobility of carbon.

Thus, despite the iron-loving behavior of C and N, fluids can be efficient carriers of volatiles even under the conditions of the metal-saturated mantle at the standard heat flux. Lower values of $D_C^{Me/Fl}$ than $D_N^{Me/Fl}$ indicate that fluid–metal interactions lead to the selective accumulation of nitrogen by the metal phase (solid iron or metal melt). Carbon mainly resides in the HC species of the fluid phase and can be transported to the shallow mantle. This process may become faster as a result of the selective synthesis of C-rich heavy HCs catalyzed by the metal melt.

Conclusions

The Fe–C–O–H–N system has been investigated experimentally at 6.3–7.8 GPa and 1200–1400 °C, which simulate the upper mantle conditions at depths of 200–250 km with the standard heat flux of 40 mW/m². This study reveals that the γ-Fe and melt phases are stable in equilibrium with the fluid phase in a C- and N-unsaturated system. The ε-Fe_3N phase (space groups $P6_3/mmc$ or $P6_322$) forms in an N-rich system at graphite saturation in subsolidus conditions, at 1200–1300 °C, while N-rich melts appear at 1400 °C. The fluid compositions at fH_2 buffered by IW and MMO can vary in a large range, i.e., from NH_3-rich to H_2O-rich fluids with notable amounts of alkanes. The metal melt can cause a catalytical effect on fluid composition, which leads to the predominance of oxygenated HCs. At MMO-buffered fH_2, alcohols and esters become the main carbon hosts, while carboxylic acids are predominant at unbuffered fH_2 conditions. As the contents of O-bearing HCs increase, H_2O decreases, and the fluid gains more carbon. The stability of NH_3 in a metal-bearing system depends on fH_2: NH_3 is the principal nitrogen species in the case of fH_2 at MMO or IW, but the NH_3/N_2 ratio decreases to ≤ 0.1 in unbuffered runs.

The estimated coefficients of C and N partitioning between the metal phase and the reduced fluid are < 1 in all cases (but one for nitrogen partitioning between a C- and N- unsaturated melt and a fluid). Therefore, a fluid relatively rich in C and N is stable in equilibrium with the metal phase (γ-Fe, melt, Fe_3N), though carbon and nitrogen show affinities for iron under the upper mantle P–T conditions. However, the metal/fluid partition coefficients of nitrogen are higher than those of carbon. Therefore, the nitrogen affinity for iron exceeds that of carbon under these conditions. This is demonstrated by the fact that the nitrogen-fluid reaction leads to the substitution of the initial Fe_3C for Fe_3N and carbon release when there is excess C and N in the system. The synthesis of heavy HCs in the equilibrium fluid, in the presence of a metal melt, markedly increases the C content in the fluid, as well as the difference between the melt/fluid partition coefficients of C and N. Generally, the reported results show that reduced fluids can successfully transport volatiles from the metal-saturated to metal-free shallow mantle. However, the higher nitrogen affinity for iron maintains its selective accumulation in the metal phase and high mobility of carbon in the fluid phase. This may be the mechanism that controls the carbon and nitrogen cycles in the metal-saturated mantle.

References

Abe Y (1997) Thermal and chemical evolution of the terrestrial magma ocean. Phys Earth Planet Inter 100:27–39

Bataleva YV, Palyanov YN, Borzdov YM, Sobolev NV (2016) Graphite and diamond formation via the interaction of iron carbide and Fe, Ni-sulphide under mantle P-T parameters. Dokl Earth Sci 471:1144–1148

Borzdov Y, Pal'Yanov Y, Kupriyanov I, Gusev V, Khokhryakov A, Sokol A, Efremov A (2002) HPHT synthesis of diamond with high nitrogen content from an Fe₃N-C system. Diam Relat Mater 11:1863–1867

Budde WL (2001) Analytical mass spectrometry. Strategies for environmental and related applications. Oxford University Press Oxford 386 pp

Dalou C, Hirschmann MM, von der Handt A, Mosenfelder J, Armstrong LS (2017) Nitrogen and carbon fractionation during core–mantle differentiation at shallow depth. Earth Planet Sci Lett 458:141–151

Dasgupta R (2013) Ingassing, storage, and outgassing of terrestrial carbon through geologic time. Rev Mineral Geochem 75:183–229

Dasgupta R, Hirschmann MM (2010) The deep carbon cycle and melting in Earth's interior. Earth Planet Sci Lett 298:1–13

Dasgupta R, Walker D (2008) Carbon solubility in core melts in a shallow magma ocean environment and distribution of carbon between the Earth's core and the mantle. Geochim Cosmochim Acta 72:4627–4641

Dasgupta R, Chi H, Shimizu N, Buono AS, Walker D (2013) Carbon solution and partitioning between metallic and silicate melts in a shallow magma ocean: implications for the origin and distribution of terrestrial carbon. Geochim Cosmochim Acta 102:191–212

Davis BH (2009) Fischer–Tropsch synthesis: reaction mechanisms for iron catalysts. Catal Today 141(1):25–33

Fadeeva VP, Tikhova VD, Nikulicheva ON (2008) Elemental analysis of organic compounds with the use of automated CHNS analyzers. J Anal Chem 63:1094–1106

Frost DJ, McCammon CA (2008) The redox state of Earth's mantle. Annu Rev Earth Planet Sci 36:389–420

Frost DJ, Liebske C, Langenhorst F, McCammon CA, Trønnes RG, Rubie DC (2004) Experimental evidence for the existence of iron-rich metal in the Earth's lower mantle. Nature 428:409–412

Gajbhiye NS, Bhattacharyya S, Shivaprasad SM (2008) Synthesis and characterization of ε-Fe₃N/GaN, 54/46-composite nanowires. Mater Res Bull 43:272–283

Guillermet AF, Frisk K (1991) Thermodynamic properties of Ni nitrides and phase stability in the Ni-N system. Int J Thermophys 12:417–431

Hashizume K, Kase T, Matsuda J (1997) On the siderophile behaviour of nitrogen and carbon: implications for their inventory in the Earth. Kazan 42:S293–S301

Hasterok D, Chapman DS (2011) Heat production and geotherms for the continental lithosphere. Earth Planet Sci Lett 307:59–70

Hirschmann MM (2012) Magma ocean influence on early atmosphere mass and composition. Earth Planet Sci Lett 341–344:48–57

Hirschmann MM, Dasgupta R (2009) The H/C ratios of Earth's near-surface and deep reservoirs, and consequences for deep Earth volatile cycles. Chem Geol 262:4–16

Jack KH (1948) Binary and ternary interstitial alloys. II. The iron-carbon-nitrogen system. Proc R Soc Lond A 195, 41

Jacob DE, Kronz A, Viljoen KS (2004) Cohenite, native iron and troilite inclusions in garnets from polycrystalline diamond aggregates. Contrib Mineral Petrol 146:566–576

Jacobs H, Rechenbach D, Zachwieja U (1995) Structure determination of γ'-Fe₄N and ε-Fe₃N. J Alloys Compd 227:10–17

Kadik AA, Kurovskaya NA, Ignat'ev YA, Kononkova NN, Koltashev VV, Plotnichenko VG (2011) Influence of oxygen fugacity on the solubility of nitrogen, carbon, and hydrogen in FeO-Na₂O-SiO₂-Al₂O₃ melts in equilibrium with metallic iron at 1.5 GPa and 1400 C. Geochem Inter 49:429

Kadik A, Litvin YA, Koltashev VV, Kryukova EB, Plotnichenko VG, Tsekhonya TI, Kononkova NN (2013) Solution behaviour of reduced N–H–O volatiles in FeO–Na₂O–SiO₂–Al₂O₃ melt equilibrated with molten Fe alloy at high pressure and temperature. Phys Earth Planet Inter 214:14–24

Kagawa A, Okamoto T (1981) Partition of nitrogen in hypo-eutectic and nearly eutectic iron-carbon alloys. Trans Jap Inst Met 22:137

Kaminsky FV, Wirth R (2011) Iron carbide inclusions in lower-mantle diamond from Juina, Brazil. Can Mineral 49:555–572

Kaminsky F, Wirth R (2017) Nitrides and carbonitrides from the lowermost mantle and their importance in the search for Earth's "lost" nitrogen. Am Mineral doi: https://doi.org/10.2138/am-2017-6101

Kuramoto K (1997) Accretion, core formation, H and C evolution of the Earth and Mars. Phys Earth Planet Inter 100:3–20

Kuramoto K, Matsui T (1996) Partitioning of H and C between the mantle and core during the core formation in the Earth: its implications for the atmospheric evolution and redox state of early mantle. J Geophys Res 101:14909–14932

Lebedev A (ed) (2012) Comprehensive environmental mass spectrometry. ILM Publications

Li Y, Keppler H (2014) Nitrogen speciation in mantle and crustal fluids. Geochim Cosmochim Acta 129:13–32

Li Y, Wiedenbeck M, Shcheka S, Keppler H (2013) Nitrogen solubility in upper mantle minerals. Earth Planet Sci Lett 377:311–323

Li Y, Huang R, Wiedenbeck M, Keppler H (2015) Nitrogen distribution between aqueous fluids and silicate melts. Earth Planet Sci Lett 411:218–228

Li Y, Marty B, Shcheka S, Zimmermann L, Keppler H (2016a) Nitrogen isotope fractionation during terrestrial core-mantle separation. Geochem Persp Let 2:138–147

Li Y, Dasgupta R, Tsuno K, Monteleone B, Shimizu N (2016b) Carbon and sulfur budget of the silicate earth explained by accretion of differentiated planetary embryos. Nat Geosci 9(10):781

Libourel G, Marty B, Humbert F (2003) Nitrogen solubility in basaltic melt. Part I. Effect of oxygen fugacity. Geochim Cosmochim Acta 67:4123–4135

Litasov KD, Shatskiy AF, Ohtani E (2014) Melting and subsolidus phase relations in peridotite and eclogite systems with reduced C–O–H fluid at 3–16 GPa. Earth Planet Sci Lett 391:87–99

Lord OT, Walter MJ, Dasgupta R, Walker D, Clark SM (2009) Melting in the Fe-C system to 70 GPa. Earth Planet Sci Lett 284:157–167

Luth RW (1989) Natural versus experimental control of oxidation state: effects on the composition and speciation of C–O–H fluids. Am Mineral 74:50–57

Luth RW (2014) Volatiles in Earth's mantle. Treatise on Geochemistry. Elsevier, Oxford 3.9, pp 355–391

Marty B (2012) The origins and concentrations of water, carbon, nitrogen and noble gases on earth. Earth Planet Sci Lett 313–314:56–66

McCollom TM, Ritter G, Simoneit BR (1999) Lipid synthesis under hydrothermal conditions by Fischer-Tropsch-type reactions. Origins of Life Evol Biosph 29(2):153–166

Miyazaki A, Hiyagon H, Sugiura N, Hirose K, Takahashi E (2004) Solubilities of nitrogen and noble gases in silicate melts under various oxygen fugacities: implications for the origin and degassing

history of nitrogen and noble gases in the earth. Geochim Cosmochim Acta 68:387–401

Mysen BO, Fogel ML (2010) Nitrogen and Hydrogen Isotope compositions and solubility in silicate melts in equilibrium with reduced (N + H)-bearing fluids at high pressure and temperature: effects of melt structure. Am Mineral 95:987–999

Mysen BO, Yamashita S, Chertkova N (2008) Solubility and solution mechanisms of NOH volatiles in silicate melts at high pressure and temperature—amine groups and hydrogen fugacity. Am Mineral 93:1760–1770

Oxford Diffraction (2005). CrysAlis CCD and CrysAlis RED Oxford Diffraction Ltd, Abingdon

Palyanov YuN, Borzdov YuM, Khokhryakov AF, Kupriyanov IN, Sokol AG (2010) Effect of nitrogen impurity on diamond crystal growth processes. Cryst Growth Des 10:3169–3175

Palyanov YN, Borzdov YM, Kupriyanov IN, Khokhryakov AF (2012) Effect of H_2O on diamond crystal growth in metal–carbon systems. Cryst Growth Des 12:5571–5578

Palyanov YuN, Bataleva YV, Sokol AG, Borzdov YM, Kupriyanov IN, Reutsky VN, Sobolev NV (2013) Mantle–slab interaction and redox mechanism of diamond formation. Proc Nat Acad Sci USA 110:20408–20413

Rohrbach A, Schmidt MW (2011) Redox freezing and melting in the Earth's deep mantle resulting from carbon-iron redox coupling. Nature 472:209–212

Rohrbach A, Ghosh S, Schmidt MW, Wijbrans CH, Klemme S (2014) The stability of Fe–Ni carbides in the Earth's mantle: evidence for a low Fe–Ni–C melt fraction in the deep mantle. Earth Planet Sci Lett 388:211–221

Roskosz M, Mysen BO, Cody GD (2006) Dual speciation of nitrogen in silicate melts at high pressure and temperature: an experimental study. Geochim Cosmochim Acta 70:2902–2918

Roskosz M, Bouhifd MA, Jephcoat AP, Marty B, Mysen BO (2013) Nitrogen solubility in molten metal and silicate at high pressure and temperature. Geochim Cosmochim Acta 121:15–28

Shcheka SS, Wiedenbeck M, Frost DJ, Keppler H (2006) Carbon solubility in mantle minerals. Earth Planet Sci Lett 245:730–742

Sheldrick G (2008) A short history of SHELX. Acta Crystallogr A64:112–122

Smith EM, Kopylova MG (2014) Implications of metallic iron for diamonds and nitrogen in the sub-lithospheric mantle. Can J Earth Sci 51:510–516

Smith EM, Shirey SB, Nestola F, Bullock ES, Wang J, Richardson SH, Wang W (2016) Large gem diamonds from metallic liquid in Earth's deep mantle. Science 354:1403–1405

Sobolev NV, Efimova ES, Pospelova LN (1981) Native iron in Yakutian diamonds and its mineral assemblage. Soviet Geol Geophys 22(12):25–28

Sobolev NV, Tomilenko AA, Bul'bak TA, Logvinova AM (2017) Composition of volatile components in diamonds and garnets from unique diamondiferous peridotite of the Udachnaya pipe, Yakutia, Russia. Third DCO International Science Meeting. University of St. Andrews. Scotland. p 115

Sokol AG, Palyanova GA, Palyanov YuN, Tomilenko AA, Melenevsky VN (2009) Fluid regime and diamond formation in the reduced mantle: experimental constraints. Geochim Cosmochim Acta 73:5820–5834

Sokol AG, Borzdov YuM, Palyanov YuN, Khokhryakov AF (2015) High-temperature calibration of a multi-anvil high-pressure apparatus. High Press Res 35:139–147

Sokol AG, Kruk AN, Seryotkin YV, Korablin AA, Palyanov YN (2017a) Phase relations in the $Fe-Fe_3C-Fe_3N$ system at 7.8 GPa and 1350 °C: Implications for carbon and nitrogen hosts in Fe^0-saturated upper mantle. Phys Earth Planet Inter 265:43–53

Sokol AG, Palyanov YN, Tomilenko AA, Bul'bak TA, Palyanova GA (2017b) Carbon and nitrogen speciation in nitrogen-rich C–O–H–N fluids at 5.5–7.8 GPa. Earth Planet Sci Lett 460:234–243

Sokol AG, Tomilenko AA, Bul'bak TA, Palyanova GA, Sokol IA, Palyanov YuN (2017c) Carbon and Nitrogen Speciation in N-poor C-O-H-N Fluids at 6.3 GPa and 1100–1400 °C. Sci Rep 7:706

Solomatov VS (2000) Fluid dynamics of a terrestrial magma ocean. Origin Earth Moon 323–338

Stachel T, Luth RW (2015) Diamond formation - where, when and how? Lithos 220:200–220

Stachel T, Harris JW, Brey GP (1998) Rare and unusual mineral inclusions in diamonds from Mwadui, Tanzania. Contrib Mineral Petrol 132:34–47

Strong HM, Chrenko RM (1971) Diamond growth rates and physical properties of laboratory-made diamond. J Phys Chem 75:1838–1843

Taylor WR, Green DH (1988) Measurement of reduced peridotite-COH solidus and implications for redox melting of the mantle. Nature 332:349–352

Tomilenko AA, Chepurov AI, Pal'yanov YN, Pokhilenko LN, Shebanin AP (1997) Volatile components in the upper mantle (from data on fluid inclusions). Russian Geology and Geophysics c/c of Geol Geofiz 38:294–303

Tomilenko AA, Chepurov AI, Pal'Yanov YN, Shebanin AP, Sobolev NV (1998) Hydrocarbon inclusions in synthetic diamonds. Eur J Mineral 10(6):1135–1141

Tomilenko AA, Ragozin AL, Shatskii VS, Shebanin AP (2001) Variation in the fluid phase composition in the process of natural diamond crystallization. Dokl Earth Sci 379:571–574